Silicon-Based Suspended Microchannel Resonator Developed Using Au Thermal Diffusion Bonding for Mass Sensing of Biomaterials

Keita Funayama, Atsushi Miura, Fumihito Arai, *Member, IEEE*, and Hiroya Tanaka, *Senior Member, IEEE*

***Abstract*— Suspended microchannels are of great interest in applications such as physical and chemical sensor systems. In this study, we developed a suspended microchannel resonator (SMR) by bonding two separate Au-coated silicon–insulator–silicon substrates via thermal diffusion bonding. To obtain a secure bond between Au films, we investigated different bonding temperatures and Au film thicknesses. As a result, we successfully fabricated an SMR. We show that the developed resonator has a resonance frequency of 229.55 kHz and a quality factor of 171 for the empty channel. The response of the channel to absolute mass was 18.7 pg/Hz. The measurement results were in good agreement with the results of numerical simulations. In addition, we estimated the practical mass detectability of the developed SMR via statistical analysis. The developed SMR enabled mass detection with a resolution of 710.6 pg. Our SMR can be produced via typical semiconductor fabrication technology, which is advantageous in terms of mass production. [2023-0164]**

***Index Terms*— Mass sensor, suspended microchannel resonator, micro electromechanical system, semiconductor process, thermal diffusion bonding.**

I. Introduction

MICROELECTROMECHANICAL systems (MEMSs) have attracted great attention in the field of physical and chemical sensors [1], [2]. In addition, suspended microchannel resonators (SMRs) have been developed for sensing biomaterials because their resonance frequency is highly sensitive, thereby enabling the detection of nano/microscale materials [3], [4], [5]. Burg et al. have reported an SMR with resonance frequency of 426.8 kHz, mass resolution of 2.7×10^{-20} kg in 1 kHz bandwidth, and a quality factor of approximately 9000, where the device was surrounded by a vacuum and filled with nitrogen gas [6]. Barton et al. have shown a suspended polysilicon doubly clamped beam with a resonance frequency of 25 MHz and a quality factor of 2900 for an empty channel [7]. The sensing capability of the nanochannel resonators was 103 Hz/fg. These devices can be used to determine the mass of biomaterials such as single bacterial cells and single nanoparticles.

Biomaterials are immobilized on the inside surface wall of the SMR, and their masses are detected as a change in the resonance frequency resulting from a change in the SMR's effective mass. SMRs have been produced using several processes, including bonding of two substrates [8], [9], [10] and etching of sacrificial materials [7], [11], [12], [13], [14]. In particular, fabrication based on the two-substrate bonding method is advantageous with respect manufacturing at low temperatures and controlling the channel dimensions and shape. This advantage stems from the process being conducted using mature semiconductor fabrication technology.

Meanwhile, self-assembled monolayers (SAMs) bind to and accumulate on solid surfaces to form nanoscale thin films [15], [16], [17]. Such SAMs are widely used for immobilizing nano/micromolecules in biosensors and have been actively studied because of their easy fabrication. Thiol and disulfide derivatives are known to form dense thin films on the surface of precious metals (e.g., Au, Ag, Cu, Pd, and Pt). In particular, SAMs formed by thiols and disulfides on Au substrates are commonly used in biosensors such as surface plasmon resonance (SPR) spectrometers [18], [19] and quartz crystal microbalances (QCMs) [20], [21], [22], [23]. Given this background information, the interior wall of the hollow beam in SMRs should have a Au surface, like the substrates used in SPR and QCMs, to immobilize the nano/microscale materials.

In the present study, we fabricated SMRs by joining two separate Au-coated silicon–on–insulator (SOI) substrates with Au-Au thermal diffusion bonding, which is a welding technique to create a joint between materials [24], [25]. We investigated different bonding temperatures and Au film thicknesses to attain a robust bond between the Au films. As a result, we successfully fabricated an SMR with a Au-coated channel wall. The developed SMR had a resonance frequency of 229.55 kHz and a quality factor of 171 for the empty channel at normal temperature and pressure. We found that the response of the channel to absolute mass was 18.7 pg/Hz. The measurement results were in good agreement with the

Manuscript received 8 September 2023; revised 19 December 2023; accepted 4 January 2024. Date of publication 22 January 2024; date of current version 4 April 2024. This work was supported in part by the Nagoya University Microstructural Characterization Platform as a Program of "Advanced Research Infrastructure for Materials and Nanotechnology in Japan (ARIM)" of the Ministry of Education, Culture, Sports, Science and Technology (MEXT), Japan. Subject Editor R. N. Candler. *(Corresponding author: Keita Funayama.)*

Keita Funayama, Atsushi Miura, and Hiroya Tanaka are with the Toyota Central Research and Development Laboratories Inc., Aichi 480-1192, Japan (e-mail: funayama@mosk.tytlabs.co.jp a-miura@mosk.tytlabs.co.jp; tanak@mosk.tytlabs.co.jp;).

Fumihito Arai is with Department of Mechanical Engineering, The University of Tokyo, Tokyo 113-8654, Japan (e-mail: arai-fumihito@g.ecc.u-tokyo.ac.jp).

Color versions of one or more figures in this article are available at https://doi.org/10.1109/JMEMS.2024.3352835.

Digital Object Identifier 10.1109/JMEMS.2024.3352835

results obtained using a numerical simulation. In addition, we estimated the practical mass detectability of the developed SMR via statistical analysis, and found that it enables mass detection with a resolution of 710.6 pg.

Importantly, in our proposed SMR, the Au film coated on the substrate plays two roles: (i) as the Au–Au bonding material and (ii) as the S–Au bonding material. The first role is critical for the bonding of two substrates because our SMR is fabricated via Au–Au thermal diffusion bonding, which enables the substrates to be joined at low temperatures. Low-temperature joining minimizes thermal damage to the substrates. Actually, our process provides a fine bond at 200 °C, which is lower than the melting temperature of Au. The second role is important for the immobilization of biomaterials. The formation of an organosulfur monolayer on the Au surface is preferable because such monolayers are easy to prepare and because of the high stability imparted by the strength of the S–Au bond as a result of van der Waals interactions. Moreover, Au is an inert and biocompatible material that is easy to acquire. Our process provides a Au-coated channel wall that enables the easy fabrication of SAMs on the inner wall in an SMR.

The remainder of this paper is organized as follows. In Section II, we explain the mass-sensing mechanism for SMRs. We then present details of the fabrication process in Section III. In Section IV, we specify the conditions for obtaining a fine bond in Au–Au thermal diffusion bonding. In Section V, we discuss the resonance frequency and quality factor for the developed SMR. We also calculate the minimal detectable mass. We conclude with some final remarks in Section VI.

II. Principle of Mass Sensing via Suspended Microchannel Resonators

We begin with a brief explanation of the biomaterial sensing mechanism for SMRs, which is illustrated in Fig. 1. Au is coated over the channel wall in the resonator. Organosulfur compounds form self-assembled monolayers on Au [26], and the resulting assemblies are often used as a bioprobe to immobilize biomaterials. When a solution containing biomaterials flows through the channel, the biomaterials are immobilized on the wall surface of the SMR. The mass of the immobilized biomaterial can then be determined by measuring the shift in the SMR's resonance frequency.

To explain the operating principle of SMRs in detail, we consider the mass–spring equation. The resonance frequency f_0 for an SMR including the solvent alone (refer to the top-left panel in Fig. 1) is given by

$$f_0 = \frac{1}{2\pi}\sqrt{\frac{k}{m}}, \tag{1}$$

where k is the spring constant and m is the effective mass. When biomaterials are immobilized on the interior wall of an SMR (bottom-left panel in Fig. 1), the change in mass, $\Delta m \in \mathbb{R}^+$, translates into a shift in the resonance frequency, $\Delta f \in \mathbb{R}^+$:

$$f_0 - \Delta f = \frac{1}{2\pi}\sqrt{\frac{k}{m+\Delta m}}. \tag{2}$$

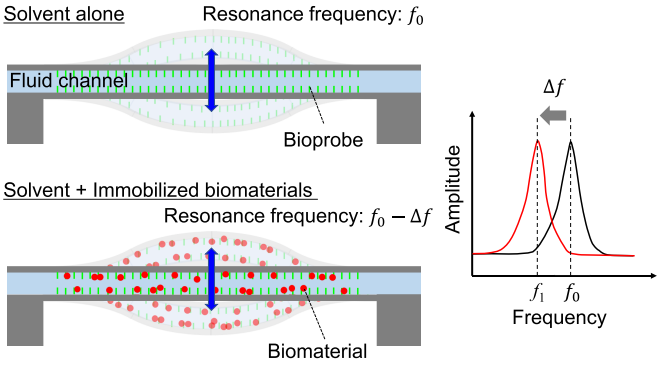

Fig. 1. Mass-sensing mechanism for SMR.

When we know the mass of the solution as a reference, we can calculate Δm from (1) and (2).

We note the treatment of the spring constant k in (1) and (2). The spring constant is associated with temperature and stress, which affect the resonant frequency and sensitivity of the SMR. However, when measurements are conducted in the same environment, the spring constant can be treated as invariable. Moreover, the immobilized biomaterials have little effect on the spring constant because the stiffness of the immobilized biomaterials differs substantially from that of the SOI wafer, i.e., the biomaterial is more flexible than the wafer.

III. Fabrication Process

We formed the buried microchannel in the suspended resonator via a semiconductor process. Figure 2 illustrates the SMR considered in this case. To create the hollow resonator, we prepared two Au-coated SOI substrates and then joined them via thermal diffusion bonding. Photolithography and dry etching were used to fabricate the channel on the first (bottom) substrate to create the trench that patterns the stream of the microchannel. The channel on the bottom substrate was then sealed by the second (top) substrate. The thicknesses of the bottom (top) substrate for the device layer, the buried SiO_2, and the base substrate were 8 μm (3 μm), 2 μm (2 μm), and 250 μm (250 μm), respectively. Figure 3 shows a summary of the fabrication process. The process started with defining a marker recess on the surface of the substrates as an alignment guide for the subsequent lithography and bonding processes. The bottom and top substrates were then processed as follows.

A. Process for Bottom Substrate

The channel and inlets (and outlets) were etched to a depth of 5 μm via reactive-ion etching (RIE) using the Bosch process with SF_6 gas at an etching power of 1250 W and a pressure of 4.0 Pa (MUC-21 ASE-Pegasus, Sumitomo Precision Products) [Fig. 3(a)]. We also created a recess of 8 μm using RIE to form the pattern for the suspended resonator [Fig. 3(b)]. The device layer was then coated with 5 nm Cr and 500 nm Au films via magnetron sputtering with sputter equipment (SPM-403L, Tokki); sputtering of Cr and Au was conducted at a power of 100 W and 1 kW, respectively, at a pressure of 5×10^{-1} Pa in an Ar gas flow of 50 sccm [Fig. 3(c)]. The Au film on the SiO_2 layer was removed by chemical etching [Fig. 3(d)].

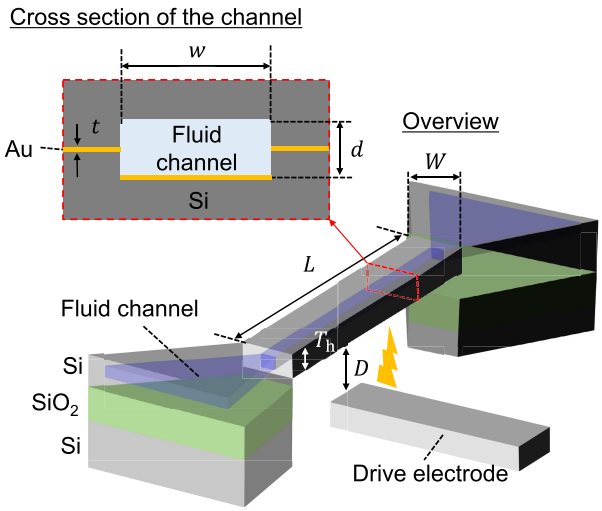

Fig. 2. Schematics of suspended microchannel. The size of the resonator was $W = 140$ μm, $L = 600$ μm, $T_h = 12$ μm, $w = 60$ μm, $t = 500$ nm, and $d = 5$ μm. The device electrode was placed at $D = 2$ μm to induce vibration to the resonator. The top-left top panel is a cross section of the beam. The sidewall thickness of the channel was 40 μm to prevent sealing failure as a result of alignment error.

B. Process for Top Substrate

In addition to forming the bottom substrate, we used RIE to form inlets (outlets) and a cover to cap the channel at a depth of 3 μm [Fig. 3(e)]. Also, 5 nm Cr and 500 nm Au thin films were deposited via magnetron sputtering onto the whole surface [Fig. 3(f)] and were subsequently removed except for a patterned Au film on the device layer [Fig. 3(g)].

C. Process for Bonding and Suspension

We cleaned the bottom and top substrates by dipping for 10 min with the piranha solution (i.e., 4:1 mixture of H_2SO_4 and H_2O_2). After being rinsed with DI water and dried by nitrogen air blow, the bottom and top substrates were joined via solid-state diffusion bonding of the deposited Au films at a pressure of 230 MPa and a temperature of 200 °C over 60 min using nanoimprint equipment (SCIVAX, X-300 BVU-ND) [Fig. 3(i)]. The bonded substrate was then etched to fabricate the inlet/outlet, beam, and driving electrode [Fig. 3(j)]. The remaining SiO_2 layers were then etched with buffered hydrofluoric acid, and part of the buried resonator was suspended [Fig. 3(k)]. Finally, the device was dried in supercritical liquid of hydrofluoroether at a pressure of 2.6 MPa and a temperature of 200 °C over 10 min.

IV. Solid-State Diffusion Bonding of Au Films

As described in the previous section, we bonded the top substrate to the bottom via thermal diffusion bonding of Au films deposited onto the substrates. Solid-state diffusion bonding should be conducted at an appropriate temperature and pressure to avoid destruction and peeling of the substrates. The purpose of this section is to specify the operating parameters for the Au–Au thermal diffusion bonding that enabled the successful fabrication of an SMR.

TABLE I
Summary of Au–Au Bonding Results

Thickness of Au (nm)	Temperature (°C)		
	200	300	400
50	+	n/a	n/a
100	+	—	—
500	++	n/a	n/a
1000	++	n/a	n/a

++: A secure bonding interface was attained.
+: The substrates were partly not jointed.
—: Voids exist at the bonding interface, and the samples were broken during the etching processes.
n/a: Not applicable.

A. Conditions

We investigated the effect of the thickness of the deposited Au, h, and the temperature during the Au–Au diffusion bonding process, T. We used two Si substrates to elucidate the fundamental properties. One substrate had a Au film evenly coated over the whole surface, and the other substrate had a sparse Au line pattern [Fig. 4(a)] because we aimed to use the sparse Au line pattern to control the pressure applied during the bonding process. More specifically, we applied $F = 41{,}000$ N to the whole surface of the top substrate, which, according to the relation $P = F/S$, gave $P = 230$ MPa on the contact area S of Au on both substrates. The pressure was set referring to the prior literature [24].

Thermal diffusion bonding is typically achieved at a temperature lower than the absolute melting temperature of the materials. We carried out thermal diffusion bonding at 200 °C, 300 °C, and 400 °C for specimens with a Au film thickness of 100 nm. We also conducted experiments using a thermal bonding temperature of 200 °C and specimens with Au film thicknesses of 50 nm, 100 nm, 500 nm, and 1000 nm. We examined the durability of the bonded substrate and visually inspected part of the Au–Au interface using cross-sectional scanning electron microscopy (SEM) images of the bonded substrates.

B. Results

We summarize the test results in Table I. We attained a secure bonding interface for a Au film thickness of 500 nm (and 1000 nm) and a thermal bonding temperature of 200 °C. Figure 4(b) shows a cross section of the bonding interface as an example of the fine samples. For the specimens prepared under the other investigated parameters, the bonding process failed. For the specimen prepared with a thickness of $h = 100$ nm and a bonding temperature of $T = 300$ °C (and 400 °C), we observed a void at the bonding interface. Moreover, the specimens were broken during the cleaning and etching processes. These results are attributed to Au readily aggregating as a result of high-temperature deformation above 300 °C, which resulted in the observed voids at the bonding interface. Moreover, for the specimens prepared with a film thickness of $h = 50$ nm and at a bonding temperature of $T = 200$ °C, the substrates were partly not joined because inadequate Au was distributed over the bonding area.

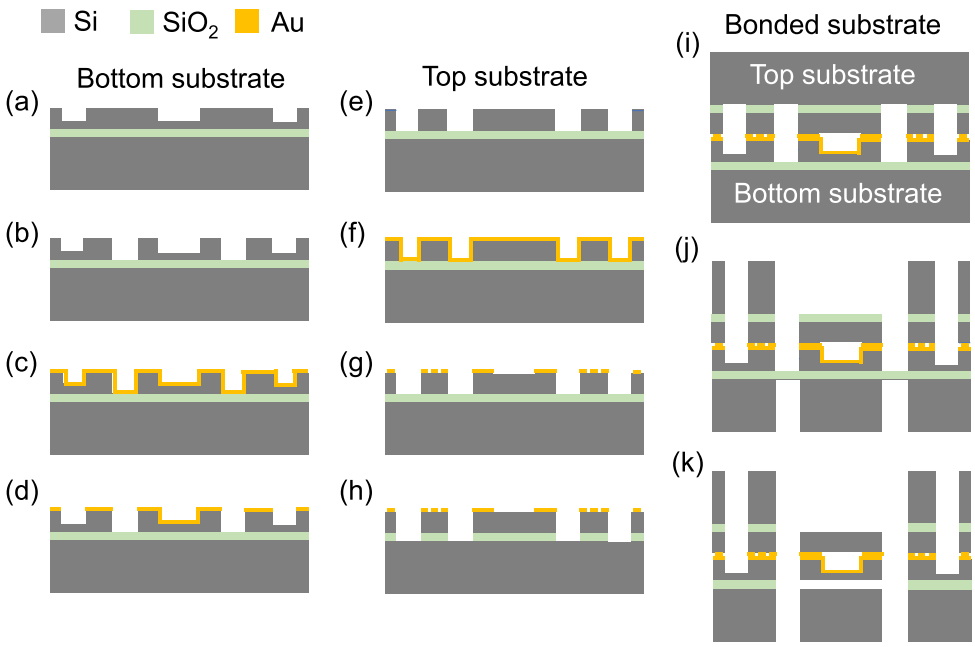

Fig. 3. Fabrication process for (a)–(d) bottom, (e)–(h) top, and (i)–(k) bonded substrates.

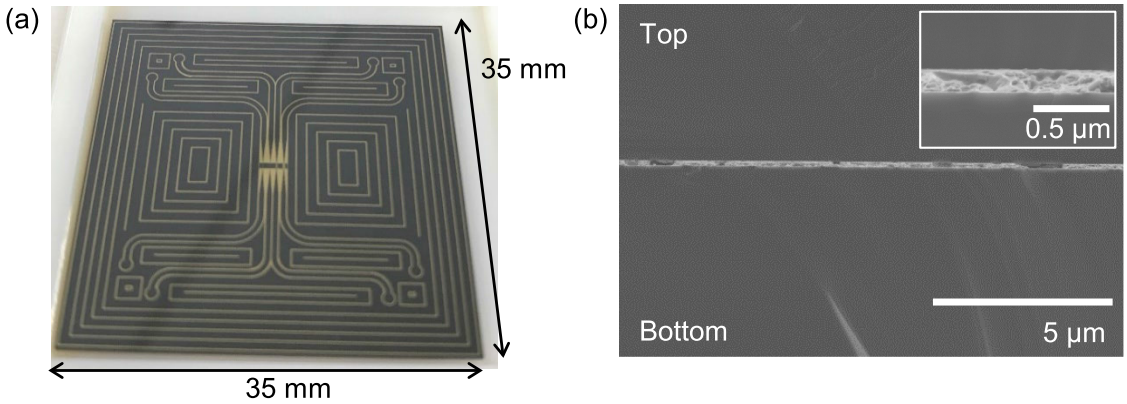

Fig. 4. (a) Au line pattern on top substrate. (b) SEM images of a cross section of a bonded interface after two substrates are joined under conditions of a 500 nm thick Au layer and a temperature of 200 °C. The inset shows an enlarged view of the interface.

From (1) and (2), the frequency shift is given by

$$\Delta f = f_0\left(1 - \sqrt{\frac{1}{1+\frac{\Delta m}{m}}}\right). \tag{3}$$

Equation (3) suggests that the observable frequency shift depends on the resonator mass m. Thus, the mass m is a key parameter affecting the sensitivity of an SMR. Specifically, when the resonator mass m is smaller, the frequency shift is larger even though the change in mass is slight. This result means that a lower resolution is acceptable for the instrumentation used for the frequency measurement.

On the basis of the above discussion, we should reduce the thickness of the Au film because the mass density of Au is much higher than that of Si. Again, a secure interface was observed for the resonators with a Au film thickness of $h = 500$ nm or $h = 1000$ nm. We used the bonding condition of $h = 500$ nm rather than $h = 1000$ nm in our fabrication process to reduce the resonator mass. Notably, when $h = 500$ nm, we expected the mass of the fabricated SMR to be 21.6% smaller than that of the SMR with $h = 1000$ nm; that is, the total resonator weight was 2.15 μg for the SMR with $h = 500$ nm and 2.61 μg for the SMR with $h = 1000$ nm.

V. Characterization Results for Fabricated SMR

Here, we present the measurement setup and design specifications for the SMR. We then present the measurement results for the fabricated resonator. Finally, we discuss the practical mass detection limit for the fabricated SMR.

A. Measurement Setup

Figure 5(a) shows the setup used to measure the vibration amplitude of the suspended microchannel. All of the fabricated devices were measured at normal temperature and pressure. A function generator (RIGOL, DG972), a stable direct-current power supply (Kikusui Electronics Corporation, PMX110-0.6 A), and a bias tee (Tektronix Keithley Instruments, PSPL5530B) were used to apply a continuous sinusoidal

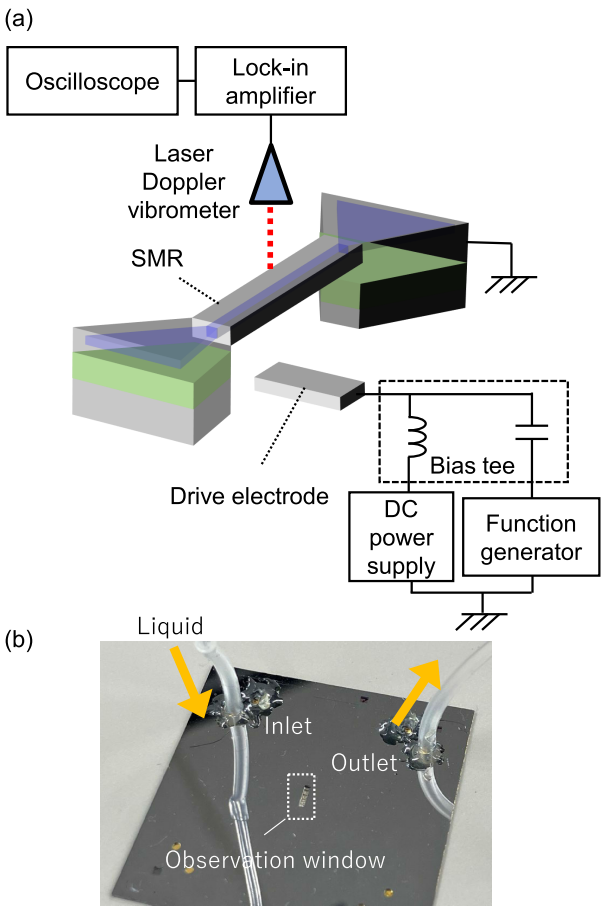

Fig. 5. (a) SMR vibration measurement setup. (b) Overview of substrate and solution infusion.

electrical signal to the device electrode to induce vibration on the suspended microchannel. The vibration velocity in the suspended channel was detected by a laser Doppler vibrometer (Ono Sokki, LV-1800); the signal was filtered and amplified by a lock-in amplifier (NF Corporation, LI5660). The amplitude of the perpendicular vibration was displayed by a digital oscilloscope (Tektronix, MSO64B). We used a four-axis stage controller (Sigmakoki, VSGSP60(XY), VSGSP60 (Z), and SHOT-304GS) to externally control the position of the test device.

Figure 5(b) shows a photograph of the inlet and outlet of the device. Silicon tubes were glued to the inlet and outlet, and the solution was infused into the channel. The resonator could be directly observed at the center of the substrate, where an observation window was located.

B. Simulation

We numerically investigated the resonator using the finite element method simulator COMSOL Multiphysics [27]. We analyzed the eigenfrequencies for the mechanical structures of the SMR. The dimensions of the resonator were 140 μm $\times$ 600 μm $\times$ 11 μm, and those of the internal channel were 60 μm $\times$ 600 μm $\times$ 5 μm. Thickness of the Au layer was 370 nm, which was adjusted to match the resonance frequency of the simulation to that of the

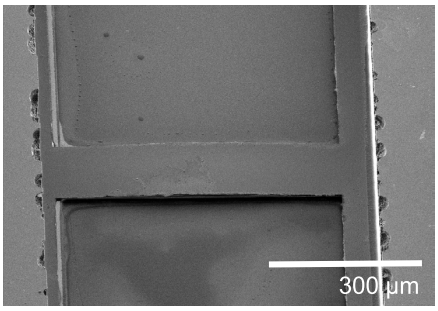

Fig. 6. SEM image of fabricated device.

TABLE II
EIGENFREQUENCY AND QUALITY FACTOR

	Solution in channel		
	Empty	Water	IPA
Eigenfrequency (kHz)	229.55	206.53	212.03
Quality factor	171	103	99

measurement. The mass densities in the simulation were set as 2.329 $\times 10^3$ kg/m^3 for Si and 1.93 $\times 10^4$ kg/m^3 for Au. The first eigenfrequency was 229.74 kHz, and the displacement was strongly amplified at this frequency.

C. Device Characteristics

1) Fundamental: Figure 6 shows a SEM image of the developed SMR. The image visually confirms that the SMR was successfully fabricated using the proposed process.

We deduced the fundamental properties of the fabricated SMR by measuring the bulk fluid mass of water and isopropyl alcohol (IPA). Figure 7(a) shows the vibration amplitude as a function of the frequency of the voltage applied to the driving electrode. The eigenfrequency is clearly shifted to lower values depending on the type of solution in the microchannel. This shift is attributable to the solution in the channel increasing the total mass of the beam. Table II shows the resonance frequency and the quality factor. We fitted the acquired data to a Lorentzian function in the calculation of the resonance frequency. The best fits are plotted as solid lines in Fig. 7(a). For the empty channel, the resonance frequency was determined to be 229.55 kHz, which is in good agreement with the value obtained in the simulation (i.e., 229.74 kHz).

The quality factor decreased when the solution was loaded into the SMR because the channel became dispersive as a result of friction between the inside wall and the contained liquid. Such dispersive behavior has been noted in previous studies [7], [11]. In addition, self-assembled monolayers will contribute to the dissipation of the SMR vibration as well as the liquid when sensing the biomaterials.

Considering the frequency shift and (3), we calculated the mass of the water and IPA in the channel. The calculated masses are plotted in Fig. 7(b). The mass of the solution in the channel was 259.5 ng for IPA and 354.9 ng for water. In addition, we calculated the sensing ability of the developed SMR in a noiseless environment. The sensing ability depends on the SMR's response to absolute mass. From the slope of the linear fit [refer to the solid line in Fig. 7(b)],

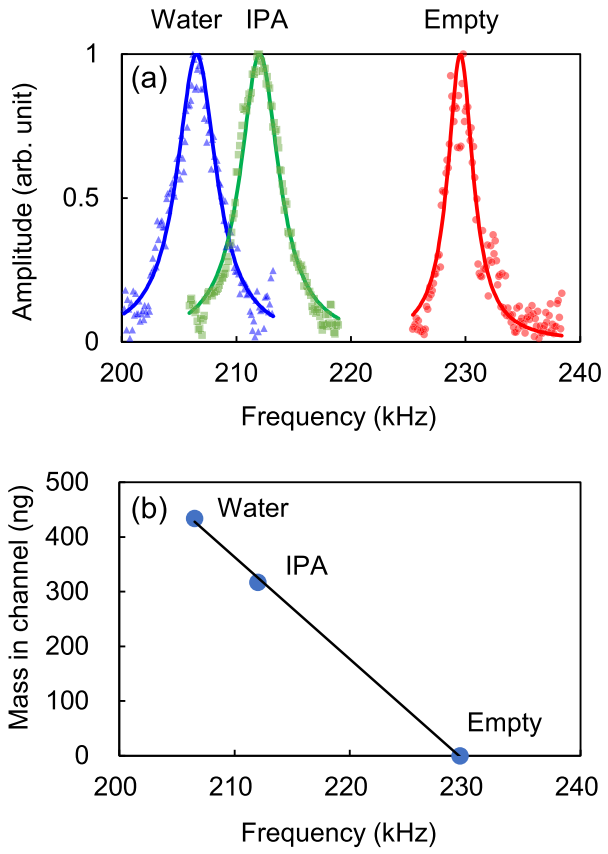

Fig. 7. (a) Vibration amplitude of fabricated SMR as function of driving frequency. Markers indicate the acquired frequency spectra, and solid lines show the spectra fitted using a Lorentzian function (red: empty; blue: water; green: IPA). (b) Mass contained in channel as the function of peak frequency. The solid line is a linear fit.

we found that the response of the channel to the absolute mass is $\frac{dm}{df} = 18.7$ pg/Hz.

From the channel volume of the SMR (600 μm $\times$ 60 μm $\times$ 5 μm) and nominal mass density of the liquids (786 kg/m^3 for IPA and 997 kg/m^3 for water), we can theoretically predict the mass of the filled IPA and water to be 141 ng and 179 ng, respectively. A discrepancy exists between the measured and theoretically predicted masses. We speculate that this discrepancy arose from the prediction error of the SMR mass, as follows. The estimated thicknesses of the Au and Cr layers would differ from those of the fabricated SMR because of an apparent fabrication error in the sputtering process, despite the sputtering process being carefully controlled. Thus, the thicknesses of the Au and Cr layers were smaller than the value used in the mass calculation. In addition, according to the SEM image in Fig. 6, the size of the resonator was smaller than the designed one because of the over-etch of the Si layer. As a result, the mass calculated from our measurement result was not perfectly matched with that obtained from the nominal mass density. Again, (3) suggests that the observable frequency shift strongly depends on the resonator mass m. Hence, for precise measurement of the mass change Δm, we should deduce the correct size of the materials (i.e., Si, Au, and Cr) in the SMR; this deduction will constitute one aspect of our future studies.

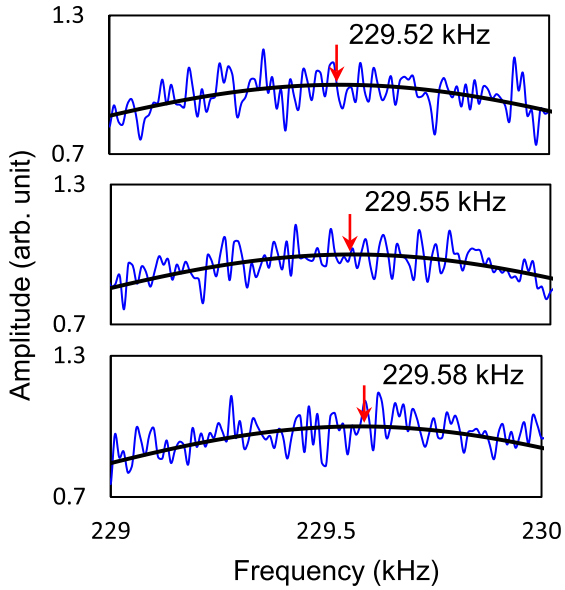

Fig. 8. Three examples of numerically generated frequency spectra corresponding to frequencies similar to resonance frequency $f = 229.55$ kHz (blue lines). The black solid line shows the fitted spectrum $g_{\rm fit}(f)$. The arrow in each figure points to the frequency $f_{\rm max}$ providing the maximum amplitude.

2) Practical Lower Mass Detection Limit: Because we acquired the frequency spectra in Fig. 7(a) at atmospheric pressure and room temperature, the spectra had blunted peaks and fluctuations resulting from dissipation and thermal noise. To this end, SMRs have a discernable mass detection range (i.e., a resolution). Here, we aim to reveal the practical resolution of the developed SMR.

For this purpose, the frequency spectrum is modeled as follows. We have the measured frequency spectrum $s(j)$ for the empty SMR [see red circles Fig. 7(a)], where $j \equiv f_{\rm low} + i\delta$ is the sampling frequency, $f_{\rm low}$ is the lower bound of the observation frequency, $i = 1, \cdots, I$ is the sampling point, and δ is the step size during sampling. In addition, we have the fitting curve $g(f)$ as a function of frequency f [red solid line in Fig. 7(a)]. Assuming that the noise $n(f)$ has a Gaussian distribution for any f, the frequency spectrum for the empty channel is written as

$$g(f) + n(f). \tag{4}$$

The noise $n(f)$ is described using the Gaussian distribution $\mathcal{N}(0, \sigma^2)$, where σ^2 is the variance. The variance σ^2 can be extracted from the dataset $\{s(j) - g(j)\}$ over all sampling points: $\sigma^2 = 6.80 \times 10^{-5}$ Hz^{-1} for the empty channel.

We can then generate multiple spectra via Monte Carlo experiments, enabling us to estimate the possible mass resolution. Specifically, we estimate the resolution from the confidence interval of the frequency providing the maximum amplitude; this confidence interval can be reliably discerned from numerical experiment data with a certain level of confidence. Figure 8 shows examples of the frequency spectra generated using (4). In addition, we plot the fitting curves $g_{\rm fit}(f)$. The maximum amplitude, $f_{\rm max} = \arg\max_f g_{\rm fit}(f)$, exists at different frequencies for each sample because of the fluctuation resulting from the noise. Figure 9 shows a

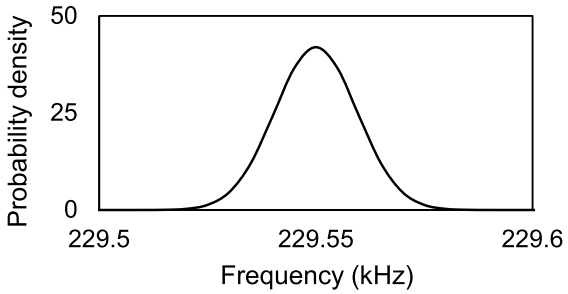

Fig. 9. Probability distribution for $f_{\max}$, which is assumed to be described by a Gaussian distribution function. The mean and variance were extracted from 1000 numerically generated samples.

probability distribution extracted from 1000 samples of $f_{\max}$. Under the assumption that $f_{\max}$ has a Gaussian distribution, we calculated the 95% confidence interval as 0.038 kHz. As a result, we obtained a resolution of 710.6 pg, which was calculated from the 95% confidence interval and the response to absolute mass: 0.038 kHz $\times$ 18.7 pg/Hz.

VI. Conclusion

We have developed suspended microchannels by bonding two separate Au-coated silicon–insulator–silicon substrates. The thickness of the Au films was 500 nm. We carried out the bonding process at a temperature of 200 °C and a pressure of 230 MPa. Consequently, we successfully obtained an SMR with a resonance frequency of 229.55 kHz and a quality factor of 171 for the empty channel at normal temperature and pressure. In addition, we found that the response of the channel to absolute mass is 18.7 pg/Hz. Our suspended microchannels can be developed via typical semiconductor fabrication technology, which is advantageous in terms of mass production. The performance of the developed SMR was measured at normal temperature and pressure; thus, the dissipation will be further reduced when the SMR is used under vacuum conditions.

In future studies, we expect to further investigate device-to-device variation and reproducibility. Statistical analysis using other measures such as Allan variance is another expected aspect of our future work. Moreover, additional studies involving simulations for the whole system, including the biomaterials and liquids in the channel, are needed for the SMR-based mass detection. In addition, calibration is required to compensate for differences between measuremtnt and theoretical values in practical applications.

References

[1] Y. Zhao, L. Gu, H. Sun, X. Sha, and W. J. Li, "Physical cytometry: Detecting mass-related properties of single cells," *ACS Sensors*, vol. 7, no. 1, pp. 21–36, Jan. 2022.

[2] A. C. R. Grayson et al., "A BioMEMS review: MEMS technology for physiologically integrated devices," *Proc. IEEE*, vol. 92, no. 1, pp. 6–21, Jan. 2004.

[3] J. Kim et al., "Hollow microtube resonators via silicon self-assembly toward subattogram mass sensing applications," *Nano Lett.*, vol. 16, no. 3, pp. 1537–1545, Mar. 2016.

[4] A. De Pastina and L. G. Villanueva, "Suspended micro/nano channel resonators: A review," *J. Micromech. Microeng.*, vol. 30, no. 4, Apr. 2020, Art. no. 043001.

[5] M. M. Daryani, T. Manzaneque, J. Wei, and M. K. Ghatkesar, "Measuring nanoparticles in liquid with attogram resolution using a microfabricated glass suspended microchannel resonator," *Microsyst. Nanoeng.*, vol. 8, no. 1, p. 92, Aug. 2022.

[6] T. P. Burg, J. E. Sader, and S. R. Manalis, "Nonmonotonic energy dissipation in microfluidic resonators," *Phys. Rev. Lett.*, vol. 102, no. 22, Jun. 2009, Art. no. 228103.

[7] R. A. Barton, B. Ilic, S. S. Verbridge, B. R. Cipriany, J. M. Parpia, and H. G. Craighead, "Fabrication of a nanomechanical mass sensor containing a nanofluidic channel," *Nano Lett.*, vol. 10, no. 6, pp. 2058–2063, Jun. 2010.

[8] T. Corman, P. Enoksson, K. Norén, and G. Stemme, "A low-pressure encapsulated resonant fluid density sensor with feedback control electronics," *Meas. Sci. Technol.*, vol. 11, no. 3, pp. 205–211, Mar. 2000.

[9] T. P. Burg et al., "Vacuum-packaged suspended microchannel resonant mass sensor for biomolecular detection," *J. Microelectromech. Syst.*, vol. 15, no. 6, pp. 1466–1476, Dec. 2006.

[10] T. P. Burg et al., "Weighing of biomolecules, single cells and single nanoparticles in fluid," *Nature*, vol. 446, no. 7139, pp. 1066–1069, Apr. 2007.

[11] T. P. Burg and S. R. Manalis, "Suspended microchannel resonators for biomolecular detection," *Appl. Phys. Lett.*, vol. 83, no. 13, pp. 2698–2700, Sep. 2003.

[12] A. Alshammri et al., "Quality factor of a microchannel microresonator as a function of viscosity and its vibrational mode: An experimental and computational analysis," *IEEE Sensors J.*, vol. 23, no. 1, pp. 104–110, Jan. 2023.

[13] L. Huang et al., "Piezoelectric-AlN resonators at two-dimensional flexural modes for the density and viscosity decoupled determination of liquids," *Microsyst. Nanoeng.*, vol. 8, no. 1, p. 38, Apr. 2022.

[14] M. F. Khan et al., "Online measurement of mass density and viscosity of pL fluid samples with suspended microchannel resonator," *Sens. Actuators B, Chem.*, vol. 185, pp. 456–461, Aug. 2013.

[15] C. Vericat, M. E. Vela, G. Benitez, P. Carro, and R. C. Salvarezza, "Self-assembled monolayers of thiols and dithiols on gold: New challenges for a well-known system," *Chem. Soc. Rev.*, vol. 39, no. 5, pp. 1805–1834, 2010.

[16] S. Casalini, C. A. Bortolotti, F. Leonardi, and F. Biscarini, "Self-assembled monolayers in organic electronics," *Chem. Soc. Rev.*, vol. 46, no. 1, pp. 40–71, 2017.

[17] M. Singh, N. Kaur, and E. Comini, "The role of self-assembled monolayers in electronic devices," *J. Mater. Chem. C*, vol. 8, no. 12, pp. 3938–3955, 2020.

[18] Y. Feng, E. R. Dionne, V. Toader, G. Beaudoin, and A. Badia, "Odd-even effects in electroactive self-assembled monolayers investigated by electrochemical surface plasmon resonance and impedance spectroscopy," *J. Phys. Chem. C*, vol. 121, no. 44, pp. 24626–24640, 2017.

[19] D. D. Galvan, V. Parekh, E. Liu, E.-L. Liu, and Q. Yu, "Sensitive bacterial detection via dielectrophoretic-enhanced mass transport using surface-plasmon-resonance biosensors," *Anal. Chem.*, vol. 90, no. 24, pp. 14635–14642, Dec. 2018.

[20] W.-L. Kao, H.-Y. Chang, K.-Y. Lin, Y.-W. Lee, and J.-J. Shyue, "Effect of surface potential on the adhesion behavior of NIH3T3 cells revealed by quartz crystal microbalance with dissipation monitoring (QCM-D)," *J. Phys. Chem. C*, vol. 121, no. 1, pp. 533–541, Jan. 2017.

[21] L. Zhou, F. Kato, and H. Ogi, "Sensitive label-free immunoglobulin g detection using a MEMS quartz crystal microbalance biosensor with a 125 MHz wireless quartz resonator," *Jpn. J. Appl. Phys.*, vol. 60, Jul. 2021, Art. no. SDDB03.

[22] Z. Xu and Y. Luo, "Immunoglobulin-immobilized quartz crystal microbalance for Staphylococcus aureus real-time detection," *IEEE Sensors J.*, vol. 22, no. 12, pp. 11594–11601, Jun. 2022.

[23] V. M. Badiani et al., "Elucidating film loss and the role of hydrogen bonding of adsorbed redox enzymes by electrochemical quartz crystal microbalance analysis," *ACS Catal.*, vol. 12, no. 3, pp. 1886–1897, Feb. 2022.

[24] E. Higurashi and T. Suga, "Review of low-temperature bonding technologies and their application in optoelectronic devices," *IEEJ Trans. Sensors Micromachines*, vol. 134, no. 6, pp. 159–165, 2014.

[25] M. S. Goorsky et al., "Characterization of interfacial morphology of low temperature, low pressure Au-Au thermocompression bonding," *Jpn. J. Appl. Phys.*, vol. 57, no. 2S1, 2018, Art. no. 02BC03.

[26] A. Ulman, "Formation and structure of self-assembled monolayers," *Chem. Rev.*, vol. 96, no. 4, pp. 1533–1554, Jan. 1996.

[27] COMSOL AB, Stockholm, Sweden. *COMSOL Multiphysics V.6.1*. Accessed: Feb. 1, 2023. [Online]. Available: https://www.comsol.com

Keita Funayama received the B.E. and M.E. degrees in mechanical system engineering from Tohoku University, Miyagi, Japan, in 2013 and 2015, respectively, and the Ph.D. degree from Nagoya University, Aichi, Japan, in 2021. He joined the Toyota Central Research and Development Laboratories Inc., Aichi, in 2015. His research interests include nano-micro-electromechanical systems, topological wave, and diffusion systems. He is a member of the Japan Society of Applied Physics.

Atsushi Miura received the B.S. degree in electrical engineering from the Nagoya Institute of Technology, Nagoya, Japan, in 1988. Since 1982, he has been with Toyota Central Research and Development Laboratories Inc., Aichi, Japan. He is currently engaged in research and development of microfabricated devices, such as silicon microsensors. He is a member of the Japan Society of Applied Physics.

Fumihito Arai (Member, IEEE) received the Doctor of Engineering degree from Nagoya University in 1993. Since 1998, he has been an Associate Professor with Nagoya University. Since 2005, he has been a Professor with Tohoku University. Since 2010, he has been a Professor with Nagoya University. Since 2020, he has been a Professor with the Department of Mechanical Engineering, The University of Tokyo, Japan, and a Visiting Professor with Nagoya University. He was the Vice President of Technical Activities, IEEE Robotics and Automation Society (RAS) (2014–2015) and (2016–2017). He is mainly engaging in the research fields of bio-robotics, micro- and nano-robotics, MEMS, and micro- and nano-mechatoronics.

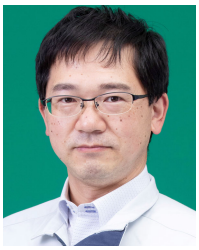

Hiroya Tanaka (Senior Member, IEEE) received the B.E. degree from Saitama University, Saitama, Japan, in 2003, and the M.E. and D.E. degrees from the Tokyo Institute of Technology, Tokyo, Japan, in 2005 and 2008, respectively. Since 2008, he has been with the Toyota Central Research and Development Laboratories Inc. His current research interests are micro/nano-structured electromagnetic devices, nonlinear signal processing, and applied radio instrumentation and measurements. He is a member of the Japan Society of Applied Physics.